Shear-induced particle migration and margination in a cellular suspension

Hong Zhao, Eric S. G. Shaqfeh, and Vivek Narsimhan

Citation: Physics of Fluids (1994-present) **24**, 011902 (2012); doi: 10.1063/1.3677935
View online: http://dx.doi.org/10.1063/1.3677935
View Table of Contents: http://scitation.aip.org/content/aip/journal/pof2/24/1?ver=pdfcov
Published by the AIP Publishing

Shear-induced particle migration and margination in a cellular suspension

Hong Zhao,[1] Eric S. G. Shaqfeh,[1,2] and Vivek Narsimhan[2]
[1]*Department of Mechanical Engineering, Stanford University, Stanford, California 94305, USA*
[2]*Department of Chemical Engineering, Stanford University, Stanford, California 94305, USA*

(Received 1 August 2011; accepted 13 December 2011; published online 31 January 2012)

We simulate the cross-flow migration of rigid particles such as platelets in a red blood cell (RBC) suspension using the Stokes flow boundary integral equation method. Two types of flow environments are investigated: a suspension undergoing a bulk shear motion and a suspension flowing in a microchannel or duct. In a cellular suspension undergoing bulk shear deformation, the cross-flow migration of particles is diffusional. The velocity fluctuations in the suspension, which are the root cause of particle migration, are analyzed in detail, including their magnitude, the autocorrelation of Lagrangian tracer points and particles, and the associated integral time scales. The orientation and morphology of red blood cells vary with the shear rate, and these in turn cause the dimensionless particle diffusivity to vary non-monotonically with the flow capillary number. By simulating RBCs and platelets flowing in a microchannel of 34 μm height, we demonstrate that the velocity fluctuations in the core cellular flow region cause the platelets to migrate diffusively in the wall normal direction. A mean lateral velocity of particles, which is most significant near the edge of the cell-free layer, further expels them toward the wall, leading to their excess concentration in the cell-free layer. The calculated shear-induced particle diffusivity in the cell-laden region is in qualitative agreement with the experimental measurements of micron-sized beads in a cylindrical tube of a comparable diameter. In a smaller duct of 10×15 μm cross section, the volume exclusion becomes the dominant mechanism for particle margination, which occurs at a much shorter time scale than the migration in the bigger channel. © *2012 American Institute of Physics*. [doi:10.1063/1.3677935]

I. INTRODUCTION

We investigate the cross-flow migration of rigid particles such as platelets in a suspension of deformable red blood cells (RBCs) under shear flow in the microcirculation. The main interest is the mechanism of platelet margination in small vessels, which results in their excess concentration in the cell-free layer near the vessel wall.[1,2] The near-wall excess of platelets is important for the rapid formation of a platelet plug at an injured vessel site,[3,4] and is hence believed to play a major role in regulating bleeding times.[4,5] Quantification of the particle migration in blood flow is also a prerequisite for modeling the transport and adsorption of drug-delivering particles *in vivo*.[6,7]

From a fluid mechanics point of view, three mechanisms are essential for the margination of platelets in a blood vessel.

- *The migration of red cells away from the vessel wall.* When an RBC is tank-treading in a wall-bound shear flow, the residual stress due to the stretch of the membrane creates a stresslet, whose interaction with the wall generates a lift velocity that pushes the cell away from the wall.[8] As cells drift away from the wall, a cell-free layer is formed known as the Fahraeus–-Lindquist effect.[9]
- *The lack of such a lift for platelets*. The platelets are much more rigid than RBCs, and thus undergo rigid-body flipping motions in the shear flow near the wall.[10] The time-averaged wall normal stresslet component is zero, and so there is no mean drift velocity in the wall normal direction.
- *A cross-flow migration of platelets due to their hydrodynamic interactions with RBCs*. We consider a binary collision between a small rigid sphere and an RBC in a simple shear flow shown

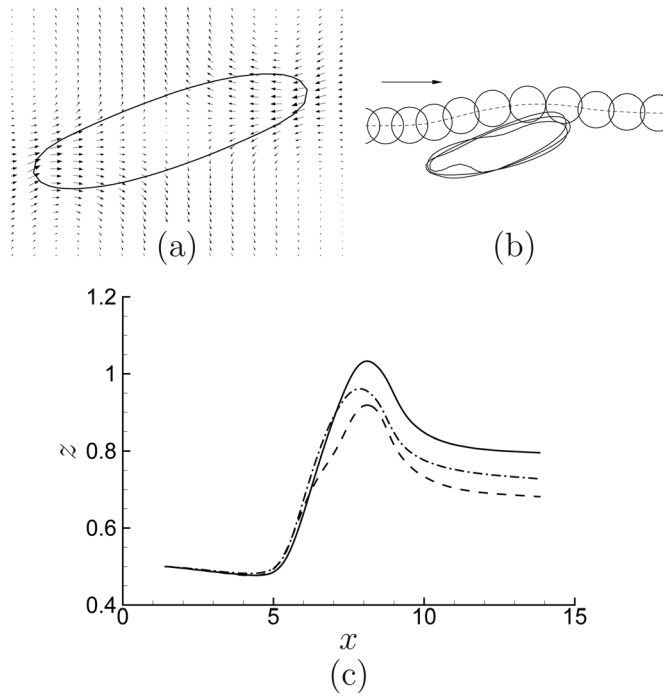

FIG. 1. (a) The perturbation velocity generated by a tank-treading RBC in a simple shear flow. (b) A spherical particle moves around an RBC in a shear flow. (c) The trajectories of the center of sphere. Each curve stands for a different random initial phase of the RBC's tank treading.

in Figure 1(b). Unlike the collision between two rigid spheres, the system here does not possess any fore-aft symmetry. This can be easily seen by the non-zero inclination angle of the RBC and its shape variation during the collision. Hence, pure hydrodynamic interaction between the two (i.e., in the absence of any contact force) can introduce a lateral migration of the rigid sphere (cf. Figure 1(c)). In an RBC/platelet suspension, the lateral migration of platelets from these collisions can be phenomenologically modeled as a shear-induced diffusion,[11,12] which is responsible for the spreading of platelets in the cell-laden region.

In a channel flow, because of the inhomogeneity in the wall normal direction, there is an additional non-zero mean lateral particle velocity. This velocity points toward the wall, and is most significant near the edge of the cell-free layer, where a platelet on average experiences more frequent collisions with RBCs from the centerline side. This mean velocity, as observed in a two-dimensional simulation[13] as well as in the present study, appears to be the major driving force for the accumulation of platelets in the cell-free layer.

In vitro experiments of perfusing RBC/platelet mixture through glass tubes and microchannels show that the presence of red blood cells is essential for the near-wall concentration of platelets. The shear-induced diffusivity enhances the platelet lateral migration speed by more than ten times when compared to their thermal diffusivity.[1,14,15] The effective wall normal diffusivity can be inferred from the platelet–wall adhesion rate based on a boundary-layer type of mass transport model,[16] and is found to approximately follow a power law with the wall shear rate.[17] These indirect measurements in general have large uncertainties so that the calculated platelet diffusivity can differ by a factor of ten under similar flow conditions.[16,17] Saadatmand *et al*. directly measure the trajectories of small spherical beads (1 μm diameter) amidst an RBC suspension in a cylindrical tube of 50 μm diameter.[18] The observed linear temporal growth of the mean square displacement of the particles in the radial direction provides direct evidence that the migration is diffusional.

To simulate the margination of platelets, Almomani *et al*. model RBCs and platelets as rigid particles of two different sizes,[19] and they observe cross-flow migration of platelets in a microchannel after they are initially released near the centerline. The suspension rheology and the hydrodynamic interactions between RBCs and platelets are, however, not representative of the

physiological system because the model does not account for the deformability of RBCs.[20] Crowl and Fogelson recently use the lattice Boltzmann method to simulate the channel flow of deformable RBCs and platelets in two dimensions.[13] They find that the lateral migration of platelets can be modeled as a convection-diffusion process: it is diffusional in the core cellular flow region with an almost constant diffusivity; near the edge of the cell-free layer, there is a significant mean drift velocity that points to the wall and thus expels the platelets into the cell-free layer. The evolution of the platelet density distribution as modeled by a stochastic differential equation is in good agreement with their direct simulation.

A similar problem is the margination of leukocytes in blood vessels and their subsequent rolling on the endothelium. Two-dimensional simulations of RBC/leukocyte in channel flows demonstrate that the RBCs push the larger and less deformable leukocytes and promote their margination to the wall.[21,22] Munn and Dupin simulate the similar problem of the segregation of cells with different membrane stiffness, and show that the cells with stiffer membranes migrate toward the peripheral of the cell-laden region because the stiffer cells have smaller wall lift velocities.[23]

In the present study, we resolve the multi-body hydrodynamic interactions in an RBC and platelet suspension by using a Stokes flow boundary integral equation method, where the RBC membrane's elasticity and bending stiffness are modeled by the finite element method. A focus here is to quantify the shear-induced diffusivity of platelets, which is determined by the magnitude of their velocity fluctuations and the velocity autocorrelations from a Lagrangian point of view. Compared to an RBC that typically has a diameter of 8 μm, the platelet has a much smaller discoid shape with a diameter of 2–5 μm and a thickness of only 0.5–1.0 μm. The platelet number density is also about 1/10 of RBCs under normal physiological conditions.[24] The velocity field is hence dominated by the RBCs, and is minimally impacted by the presence of platelets. To a first approximation regarding their self-diffusivity, the platelets can be considered as Lagrangian tracer points that are passively convected. The hypothesis is tested in two flow environments that are representative of microcirculations at different length scales: (1) a suspension undergoing bulk shear motion and (2) a suspension flowing in a microchannel or duct driven by a pressure gradient.

Our three-dimensional channel flow simulation shows that the lateral migration of platelets is characterized by their diffusion in the cell-laden region and their mean lateral migration toward the wall. Despite the qualitative similarity to the findings by Crowl and Fogelson,[13] the effective diffusivity and the mean lateral velocity obtained here are smaller by about one order of magnitude at a similar wall shear rate. In a two-dimensional system, all binary collisions between RBCs and platelets are in-plane; in three dimensions, the collisions often occur with particle centroids not in the same vorticity plane, leading to smaller cross-stream particle displacements than those found for in-plane collisions. Additionally, three-dimensional simulations are necessary for modeling the shear deformation of the RBC membrane, while in two dimensions, the membrane can have bending and extensional deformation but does not admit any shear deformation. As seen later in this paper, due to the membrane shear elasticity that is only present in three dimensions, there are significant RBC morphological changes with shear rate, which in turn cause the platelet diffusivity to have a nonlinear dependence on the shear rate.

In Sec. II, we discuss the numerical method. The simulation results are analyzed in Secs. III–V. Section VI concludes our findings.

II. NUMERICAL METHOD

Even though the blood as a whole is non-Newtonian and in particular shows significant shear-thinning at shear rates lower than 100 s^{-1},[20] the fluid phase of the blood (mainly the hemoglobin solution inside the RBC membrane and the plasma outside) is Newtonian to a good approximation. Because of the small Reynolds number in the microcirculation, we use the Stokes flow boundary integral equation method to solve the fluid velocity, where the hydrodynamic interactions between RBCs, rigid particles, and walls are represented by the convolution of Green's functions with sources distributed at the material interfaces.[25] Besides its superior accuracy, the boundary integral method is particularly convenient for the complex suspension because it obviates the difficult task of meshing the extracellular space that is three-dimensional, has a very complex geometry, and is continuously deforming.

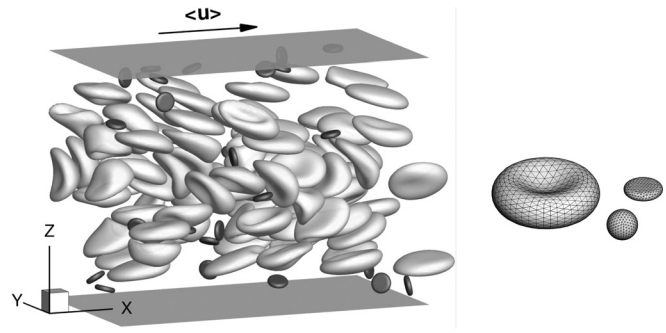

FIG. 2. Left: red blood cells and platelets in a microchannel of 34 μm in height. Right: the surface mesh used in simulation.

Figure 2 shows a suspension of RBCs and platelets flowing between two flat plates with normals in the $\pm z$ directions, where the velocity is periodic in the x and y directions. In our formulation, the flow rate is determined by specifying a background velocity $\langle \mathbf{u} \rangle$ in the x direction that is equal to the volume-averaged velocity in the computational domain (i.e., the rectangular box between the two plates). For the purpose of driving the flow, this is equivalent to specifying a mean pressure gradient $\langle \partial p/\partial x \rangle$. The ratio between $\langle u \rangle$ and $\langle \partial p/\partial x \rangle$ depends on the instantaneous suspension configuration, but in practice the fluctuation in $\langle \partial p/\partial x \rangle$ in a fully developed flow remains below 1% for constant $\langle u \rangle$. The shell of the RBC capsule is a spectrin network that is coupled to an external lipid bilayer.[26] Following the continuum approximation, we model the RBC membrane as a two-dimensional hyperelastic membrane that also resists bending deformation. We assume that the platelets are not activated and have neglected their complex surface features.[24] Since platelets are much stiffer than RBCs, they are modeled as rigid discoids that are free of external forces and torques.

To form the boundary integral equations, we first define the single-layer and double-layer integral operators for Stokes flow,

$$(\mathbf{N}\psi)_j(\mathbf{x}_0) = \int_D \psi_i(\mathbf{x}) G_{ij}(\mathbf{x}, \mathbf{x}_0) \mathrm{d}A(\mathbf{x}), \tag{1}$$

$$(\mathbf{K}\psi)_j(\mathbf{x}_0) = \int_D \psi_i(\mathbf{x}) T_{ijk}(\mathbf{x}, \mathbf{x}_0) n_k(\mathbf{x}) \mathrm{d}A(\mathbf{x}), \tag{2}$$

where the Green's functions $\mathbf{G}$ and $\mathbf{T}$ are the fundamental solutions for Stokeslet and stresslet under the periodic velocity boundary conditions.[27] The $\mathbf{G}(\mathbf{x}, \mathbf{x}_0)$ is periodic in both $\mathbf{x}$ and $\mathbf{x}_0$, and indeed only depends on $(\mathbf{x} - \mathbf{x}_0)$. The function $\mathbf{T}$ on the other hand has a decomposition,

$$T_{ijk}(\mathbf{x}, \mathbf{x}_0) = -\frac{8\pi x_j}{\Omega} \delta_{ik} + \breve{T}_{ijk}(\mathbf{x}, \mathbf{x}_0), \tag{3}$$

where $\breve{T}_{ijk}(\mathbf{x}, \mathbf{x}_0)$ is periodic. Both $\mathbf{G}$ and $\breve{\mathbf{T}}$ have zero mean in Ω so that

$$\int_\Omega \mathbf{G}(\mathbf{x}, \mathbf{x}_0) \mathrm{d}\mathbf{x} = 0 \quad \text{and} \quad \int_\Omega \breve{\mathbf{T}}(\mathbf{x}, \mathbf{x}_0) \mathrm{d}\mathbf{x} = 0. \tag{4}$$

With these constraints, the function values of $\mathbf{G}$ and $\mathbf{T}$ are uniquely determined.

Let the cell surfaces be denoted by C, the platelet surfaces by P, and the walls by W, the following boundary integral equation can be established,

$$\begin{pmatrix} \mathbf{A}_{CC} & \mathbf{A}_{CP} & \mathbf{A}_{CW} \\ \mathbf{A}_{PC} & \mathbf{A}_{PP} & \mathbf{A}_{PW} \\ \mathbf{A}_{WC} & \mathbf{A}_{WP} & \mathbf{A}_{WW} \end{pmatrix} \begin{pmatrix} \mathbf{u}_C \\ \boldsymbol{\psi}_P \\ \mathbf{f}_W \end{pmatrix} = \begin{pmatrix} \mathbf{b}_C \\ \mathbf{b}_P \\ \mathbf{b}_W \end{pmatrix}, \tag{5}$$

from which we solve for the RBC surface velocity $\mathbf{u}_C$, the wall friction force $\mathbf{f}_W$, and a double-layer density $\boldsymbol{\psi}_P$ on the surface of the platelet. The submatrices on the left-hand side are

$$\mathbf{A}_{CC} = \frac{1+\lambda}{2}\mathbf{I} - \frac{1-\lambda}{8\pi}\mathbf{K}_{CC} \qquad \mathbf{A}_{CP} = \frac{1}{8\pi}\mathbf{K}_{CP} \qquad \mathbf{A}_{CW} = \frac{1}{8\pi\mu}\mathbf{N}_{CW}$$

$$\mathbf{A}_{PC} = -\frac{1-\lambda}{8\pi}\mathbf{K}_{PC} \qquad \mathbf{A}_{PP} = \frac{1}{2}\mathbf{I} + \frac{1}{8\pi}\mathbf{K}_{PP} + \sum_{\beta=1}^{6}(\mathbf{q}''^{\beta}, \cdot)\mathbf{q}''^{\beta} \qquad \mathbf{A}_{PW} = \frac{1}{8\pi\mu}\mathbf{N}_{PW}$$

$$\mathbf{A}_{WC} = -\frac{1-\lambda}{8\pi}\mathbf{K}_{WC} \qquad \mathbf{A}_{WP} = \frac{1}{8\pi}\mathbf{K}_{WP} \qquad \mathbf{A}_{WW} = \frac{1}{8\pi\mu}\mathbf{N}_{WW},$$

and the right-hand side elements are

$$\mathbf{b}_C = -\frac{1}{8\pi\mu}\mathbf{N}_{CC}[\![\mathbf{f}]\!]_C + \langle\mathbf{u}\rangle$$
$$\mathbf{b}_P = -\frac{1}{8\pi\mu}\mathbf{N}_{PC}[\![\mathbf{f}]\!]_C + \langle\mathbf{u}\rangle$$
$$\mathbf{b}_W = -\frac{1}{8\pi\mu}\mathbf{N}_{WC}[\![\mathbf{f}]\!]_C + \langle\mathbf{u}\rangle.$$

The ratio $\lambda = \mu_{\text{inside}}/\mu_{\text{outside}}$ is between the viscosity of the hemoglobin solution inside the RBC membrane and the plasma viscosity. Each submatrix represents the hydrodynamic interaction between two sub-systems. For example,

$$(\mathbf{N}_{CW}\mathbf{f}_W)_j(\mathbf{x}_0) = \int_W \mathbf{f}_{Wi}(\mathbf{x})G_{ij}(\mathbf{x}, \mathbf{x}_0)\mathrm{d}A(\mathbf{x}) \text{ for } \mathbf{x}_0 \in C$$

is the velocity (multiplied by $8\pi\mu$) on the RBC surface induced by a wall friction force distribution $\mathbf{f}_W$. The rigid body motion of the platelets is solved by a completed double-layer formulation, and the surface velocity of any platelet is related to the double-layer density $\boldsymbol{\psi}_P$ by a projection,

$$\mathbf{u} = \sum_{\beta=1}^{6}\mathbf{q}''^{\beta}(\mathbf{q}''^{\beta}, \boldsymbol{\psi}),$$

where $\mathbf{q}''^{\beta}$ $(1 \le \beta \le 6)$ are the six orthonormal rigid body motions defined for each platelet, and $(\cdot,\cdot)$ is the standard L_2 inner product on the surface.[25]

With each surface being discretized into a mesh of linear triangles, all relevant physical quantities are approximated by piecewise linear interpolation using their mesh nodal values. The boundary integral equation (5) is discretized by a collocation method so that the residuals at all nodal points are zero upon solution, and the resulting linear equation system is solved by a generalized minimal residual (GMRES) solver. To avoid forming the dense left-hand side matrix, each matrix-vector multiplication during the solution procedure is recast as calculating the boundary integrals at collocation points. The computational cost is thus dominated by the evaluation of boundary integrals, which is accelerated by using the method of smooth particle mesh Ewald sum with $O(N \log N)$ cost.[28,29]

The elasticity of the RBC membrane is modeled by a classic two-dimensional strain energy functional.[30] The two strain invariants $I_{1,2}$ for the in-plane deformation of the unstressed membrane are

$$I_1 = \lambda_1^2 + \lambda_2^2 - 2 \quad \text{and} \quad I_2 = \lambda_1^2\lambda_2^2 - 1, \tag{6}$$

where $\lambda_{1,2}$ are the principal strains. The strain energy has the empirical form,

$$W_S = \frac{E_S}{2}\left(\frac{1}{2}I_1^2 + I_1 - I_2\right) + \frac{E_D}{8}I_2^2, \tag{7}$$

where E_S is the membrane's shear modulus and E_D is the dilatational modulus. The in-plane Cauchy stress is then,

$$\mathbf{T} = \frac{2}{J}\left(\frac{\partial W}{\partial I_1}\mathbf{F}^T\mathbf{F} + \frac{\partial W}{\partial I_2}J^2\mathbf{I}\right), \tag{8}$$

where $J = \lambda_1\lambda_2$ is the local dilatation and $\mathbf{F}$ is the deformation gradient tensor. For the linear boundary element used here, $\mathbf{F}$ and $\mathbf{T}$ are constant on each element, and one way to calculate the residual surface force $[\![\mathbf{f}]\!]$ is to differentiate $\mathbf{T}$ on the surface using discrete tensor calculus.[31] Alternatively and as is done here, the nodal values of $[\![\mathbf{f}]\!]$ can be directly calculated from a virtual work principle,

$$\delta W_S = \int_C [\![\mathbf{f}]\!] \cdot \delta\mathbf{x}\, dA(\mathbf{x}) \Rightarrow [\![\mathbf{f}]\!]_\alpha \approx \frac{1}{A_\alpha}\frac{\partial W_S}{\partial \mathbf{x}_\alpha}, \tag{9}$$

where $[\![\mathbf{f}]\!]_\alpha$ is the force density at the αth mesh node, and A_α is the surface area associated with α and is equal to 1/3 of the total area of the triangles surrounding α.

A simple bending energy formulation is used to model the membrane's bending stiffness,

$$W_B = \sum_e 2\sqrt{3}E_B[1 - cos(\beta_e - \beta_0)], \tag{10}$$

where E_B is the bending modulus, e is the edge between two neighboring surface mesh elements, and β_e is the dihedral angle formed at the edge.[32,33] The β_0 is the average bending angle for a triangular mesh over a sphere, and is estimated as $\beta_0 = [16\pi/(3\sqrt{3}N_{\text{ele}})]^{1/2}$, where N_{ele} is the number of mesh elements. The discrete values of the bending force at all mesh points are calculated by directly differentiating W_B with the coordinate of mesh points. Compared to its shear elasticity, the RBC membrane's bending resistance is weak, and its main effect lies in the suppression of surface buckling.

The volume of the red cell is $V^* = 94\,\mu\text{m}^3$, which gives an equivalent radius $a^* = (3V^*/4\pi)^{1/3} = 2.82\,\mu\text{m}$. The shape of the unstressed biconcave discocyte is described by an analytical formulation.[31] The discoid-shaped platelet has a diameter of 2.8 μm and a thickness of 0.7 μm. We have additionally simulated the dispersion of small spheres of diameter 2.26 μm. The surface meshes of RBCs and particles used in the simulations are shown in Figure 2.

All quantities are nondimensionalized by RBC radius $a^* = 2.82\,\mu\text{m}$, the plasma viscosity $\mu^* = 1.2\,\text{mPa s}$, and a characteristic shear rate $\dot{\gamma}^*$ of the flow. The RBC deformation is primarily determined by the capillary number $\text{Ca} = \mu^*\dot{\gamma}^*a^*/E_S^*$, which measures the viscous force acting on the membrane relative to its shear elasticity. For a typical value of the membrane's shear modulus $E_S = 6.8\,\mu\text{N/m}$,[34] a unit capillary number corresponds to a shear rate of approximately $2000\,\text{s}^{-1}$, which is comparable to the wall shear rate in arterioles and venules with diameters of around 30 μm.[35] The membrane's dilatational modulus $E_D^* = 10^2\mu^*\dot{\gamma}^*a^*$ is a penalty parameter; with this value of E_D^*, the area change of any RBC surface mesh element is less than 1% on average. The membrane's bending modulus is $E_B^* = 2 \times 10^{-19}\text{J}$. Since $E_B^*/(E_S^*a^{*2}) = 3.3 \times 10^{-3}$, the bending resistance is much less important than the shear elasticity.

To reduce the computational cost, the simulations are carried out with matched viscosity ($\lambda = 1$), even though physiologically the viscosity of the hemoglobin solution inside the membrane is about 5 times that of the blood plasma.[36] The motion of an isolated RBC can undergo a tank-treading to tumbling transition with such an increase in λ. In concentrated suspensions, the small intracellular space makes the rigid-body-like rotations highly unfavorable as they introduce excessive viscous dissipation. Our test simulations show that the tank-treading motion persists at $\lambda = 5$ and $\text{Ca} \geq 1$ for an RBC suspension of 20% hematocrit. Therefore, we believe using $\lambda = 5$ will not introduce qualitative changes to our present results and conclusions. A recent numerical study of RBCs flowing in small cylindrical tubes also shows insignificant changes in the flow characteristics including the cell-free layer thickness and the apparent viscosity between $\lambda = 1$ and $\lambda = 5$.[37]

III. PARTICLE DISPERSION IN AN RBC SUSPENSION UNDER SIMPLE SHEAR

In a large vessel away from both the wall boundary and the centerline, the local flow environment can be considered homogeneous and can be modeled as a cellular suspension undergoing bulk shear motion with periodic velocity boundary conditions. The characteristic shear rate $\dot{\gamma}^*$ is naturally the mean local velocity gradient, and the nondimensional background velocity of the bulk shear flow is $\mathbf{u}^\infty = (u,v,w) = (z, 0, 0)$. The model system is solved by the boundary integral

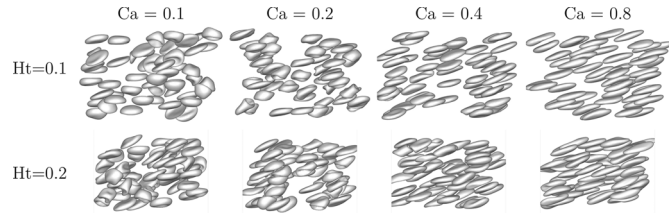

FIG. 3. RBC suspensions under bulk shear.

equation (5) with a slight modification, where we replace $\langle \mathbf{u} \rangle$ with $\mathbf{u}^{\infty}$ in the right-hand side and remove all the sub-blocks associated with the walls in the equation.

The system hematocrit (Ht) for the whole human body is between 40% and 50%, but the local hematocrit decreases significantly in small vessels and is about 16% to 20% in vessels of 30 μm diameter.[35,38] The simulation is performed at Ht = 0.1 and 0.2—the same hematocrits for the channel flow simulation as discussed in Sec. IV. The suspension in the periodic computational domain contains 54 RBCs, and an additional 20 rigid particles (spheres or platelets) when binary mixtures are simulated. Although the platelet number density is much higher than the physiologically relevant value, the hydrodynamic interactions between platelets are insignificant as compared to the platelet/RBC interactions because the platelets are dispersed among the much larger RBCs and are rarely in close contact with each other. The computational domain has a depth of $W = 12$ in the vorticity direction. Additional simulations are performed at depths of $W = 9$ and 24, and the difference in the velocity correlation curves between simulations with different W is comparable to the difference between independent simulations at the same W (cf. Figure 6).

The flow capillary number ranges between 0.1 and 2 in the simulations. Because of the inhomogeneity of its biconcave stress-free shape (dimple versus edge), an RBC cannot maintain a strictly constant shape in shear flow. Figure 3 shows significant shape variations of the cells at Ca = 0.1 and 0.2. At higher Ca (for example, Ca = 0.8 in Figure 3), the membrane's shear elasticity is dominated by the fluid viscous force, and the cell is stretched into a prolate ellipsoidal shape and undergoes a tank-treading motion,[39] which is characterized by the much reduced shape variation during its motion cycle.

The cell inclination angle ψ is defined to be between its longest axis and the flow direction, where the cell axis is identified as the eigenvector associated with the smallest eigenvalue of the cell surface's moment of inertia tensor.[40] Figure 4 shows that the Ca-dependence of $\langle \psi \rangle$ in the suspension closely follows that of an isolated cell. In Figure 3, the uniformity of ψ in the suspension becomes visually clear at Ca = 0.4, which is consistent with the significant reduction in the variation of ψ when Ca $\geq$ 0.5 in Figure 4. The fact that a cell has constant volume and surface area

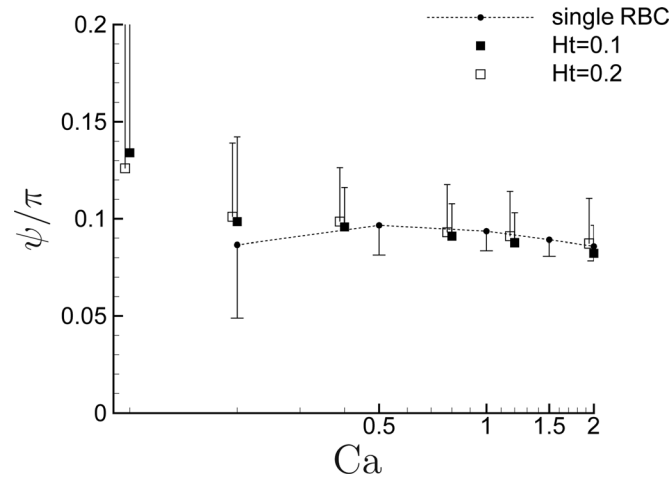

FIG. 4. The inclination angles ψ of cells (isolated and in suspension). The error bars are the variations of ψ.

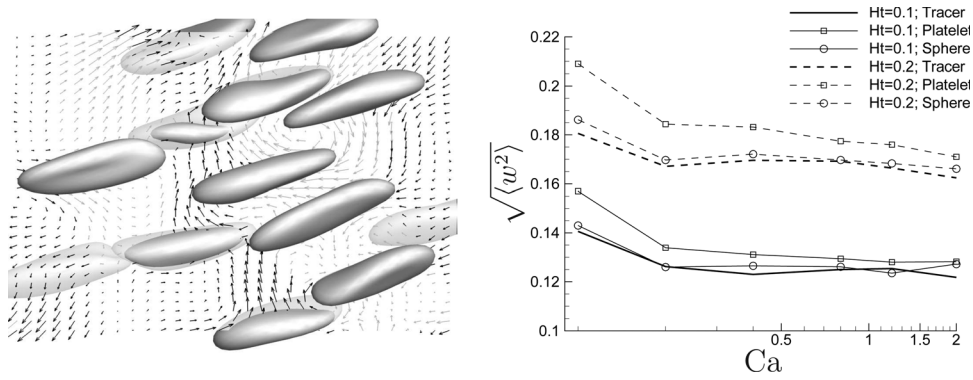

FIG. 5. Left: the disturbance velocity in the RBC suspension of Ht = 0.2 at Ca = 0.8. Right: the RMS z velocities of tracer points, small spheres, and platelets in the suspension.

determines that it cannot be stretched infinitely regardless of the Ca number. If the tank-treading shape is approximated by an ellipsoid, the ratio between the ellipsoid's longest and shortest axes has a finite upper limit that is determined by the reduced volume. Hence, the shape of the cell becomes insensitive to Ca at high shear, as shown by the weak dependence of $\langle\psi\rangle$ at large Ca in Figure 4. The variation of ψ decays monotonically with increasing Ca for an isolated cell. In a suspension, however, this variation almost remains constant because the cell–cell interactions create fluctuations that are roughly proportional to the shear rate. The comparison between Ht = 0.1 and 0.2 further shows that the variation in ψ increases at higher hematocrit due to stronger cell–cell interactions.

An instantaneous disturbance velocity field in the suspension is shown in Figure 5. Although this velocity field appears to be more chaotic than the velocity field created by an isolated cell (cf. Figure 1), both share the same key feature of contracting toward the elongated ends of cells. The root mean square (RMS) z velocity fluctuations $(\sqrt{\langle w^2\rangle})$ of Lagrangian tracer points, platelets, and spheres are also shown in Figure 5. The $\sqrt{\langle w^2\rangle}$ of tracer points decreases when Ca increases from 0.1 to 0.2, and then becomes insensitive to the change in Ca in the tank-treading regime (Ca $\geq$ 0.5). For spheres, the variation of $\sqrt{\langle w^2\rangle}$ with Ca follows closely with that of the tracer points. The $\sqrt{\langle w^2\rangle}$ of platelets follows the same trend, but is about 15% higher than that of the tracers, which is attributed to the larger dimensions of their oblate shapes.

The cross-stream migration of Lagrangian tracer points and particles is quantified by the normalized velocity autocorrelation,

$$C_z(t) = \frac{\langle w(0)w(t)\rangle}{\langle w^2\rangle}$$

and the mean square displacement,

$$\langle \Delta z^2\rangle(t) = \langle [z(t) - z(0)]^2\rangle,$$

which are shown in Figure 6 for tracers at Ht = 0.2 and Ca = 1.2. One noticeable feature is the negative correlation at $t \approx 2$, indicating a reversal of the z velocity. Observing the trajectory of a sphere passing around a tank-treading RBC in Figure 1, we note that the z coordinate of the sphere's centroid varies non-monotonically during the collision process, which would result in a similar negative velocity autocorrelation. The multiple peaks in the C_z curve indicate a sequence of encounters of a tracer point with RBCs. The $\langle \Delta z^2\rangle$ curve in Figure 6(b) shows that linear temporal growth is established at $t > 30$ despite the apparent oscillation in the slope of the curve, and so the lateral migration of tracer points is phenomenologically diffusional at this time scale. The $\langle \Delta z^2\rangle$ can be calculated alternatively using the Green–Kubo formula,

$$\langle \Delta z^2\rangle(t) = 2\langle w^2\rangle \int_0^t (t-s)C_z(s)\mathrm{d}s, \tag{11}$$

and the result is in good agreement with the direct calculation as shown in Figure 6(b).

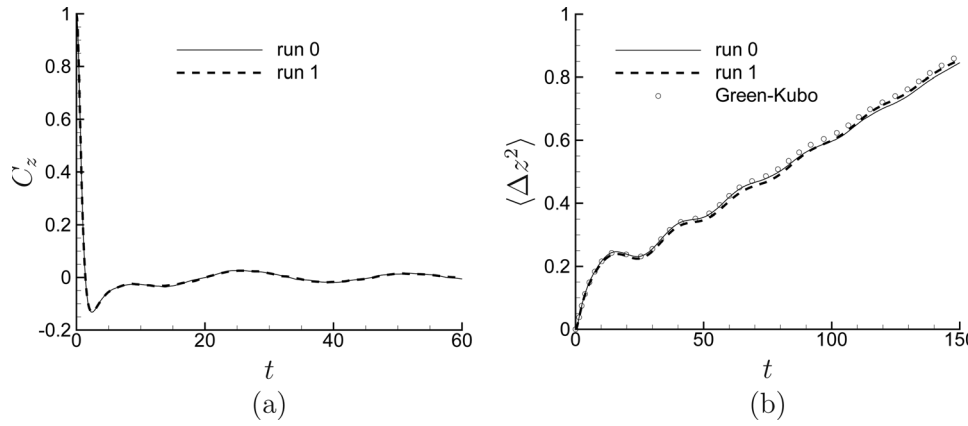

FIG. 6. (a) The z velocity autocorrelation of tracers. (b) The mean square displacement of tracers in a suspension of Ht = 0.2 and Ca = 1.2. The solid and dashed lines are the statistics obtained from two independent simulations.

Figure 7(a) compares the velocity autocorrelations of tracer points at Ht = 0.2 for three different capillary numbers. All three curves show a quantitatively similar initial decay of C_z at small t. The collision time scale, which is estimated by the occurrence of the first negative minimum of the autocorrelation, remains approximately the same at different Ca. However, the decorrelation of C_z occurs more slowly at higher Ca as there is greater similarity in the local flow environment between two consecutive collision events due to the more uniform alignment of the RBCs. This is evident from the plot of $\int_0^t C_z(s)\mathrm{d}s$ in Figure 7(b), where the oscillations in the curve increases with Ca and persists at $t > 100$ at Ca = 0.4 and 2.

The integral time scale of tracer points is calculated as $\tau = \int_0^\infty C_z(t)\,\mathrm{d}t$. Figure 8 shows that τ of tracer points is non-monotonic with Ca. The minimum τ appears to occur near Ca = 0.5 at the onset of the tank-treading regime. The integral time scale then increases with increasing Ca, but becomes less sensitive to further increase in Ca when Ca > 1. The integral time scale also decreases with increasing hematocrit in the same tank-treading regime. Therefore, the more frequent cell–cell interactions at higher hematocrit on one hand enhance the RMS fluctuating velocity $\sqrt{\langle w^2 \rangle}$ (cf. Figure 14), but on the other hand make the decorrelation occur more rapidly. These are two competing factors affecting the effective diffusivity, which is determined by,

$$D_z = \lim_{t\to\infty} \frac{1}{2}\frac{\mathrm{d}}{\mathrm{d}t}\langle [z(t) - z(0)]^2 \rangle = \langle w^2 \rangle \tau. \tag{12}$$

Figure 9(a) shows that the velocity autocorrelations of tracer points, spheres, and platelets share the similar initial decay of the correlation as well as the collision time scale—that is, the time of

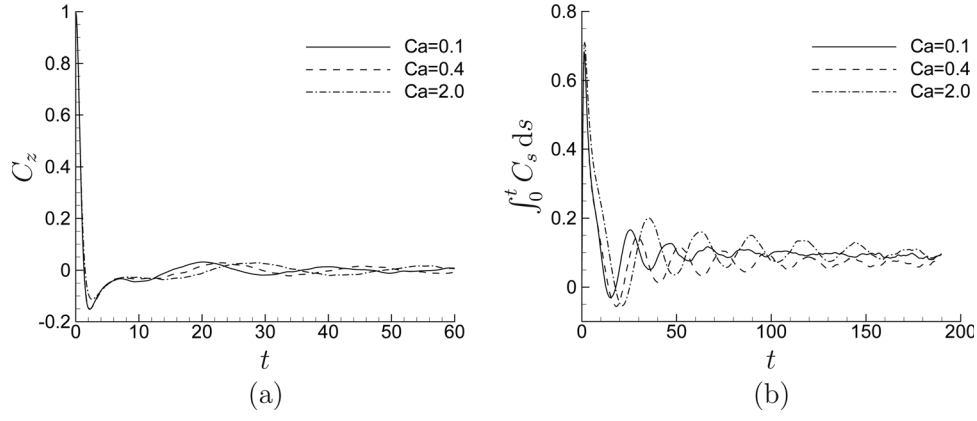

FIG. 7. (a) The velocity autocorrelation. (b) The integral time of tracer points in a suspension of Ht = 0.2 and at different capillary numbers.

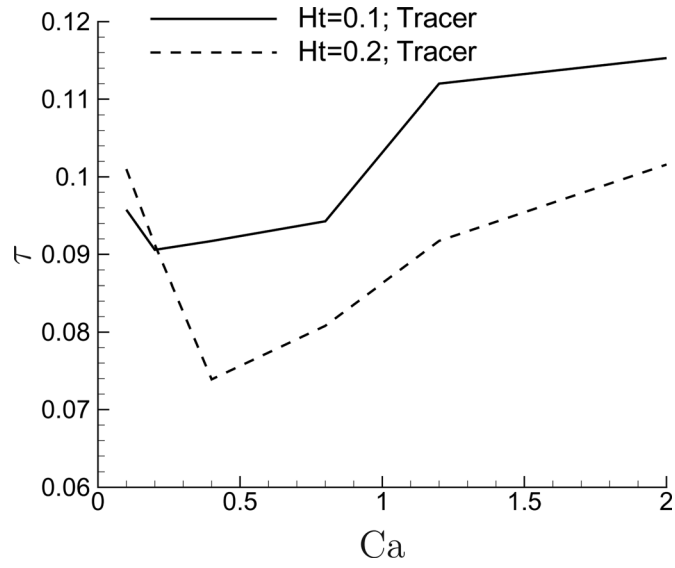

FIG. 8. The integral time scale of tracer points in the bulk shear flow.

the first negative minimum of $C_z(t)$. Spheres and platelets decorrelate faster than tracer points, with the oscillation of $C_z(t)$ already diminishing at $t > 20$, while there is still appreciable C_z for tracers at $t > 100$. This results in a more rapid establishment of the linear temporal growth of $\langle \Delta z^2 \rangle$ at $t > 20$ as shown in Figure 9(b).

The dimensionless effective shear-induced diffusivity, $D_z = D_z^*/(\dot{\gamma}^* a^{*2})$, is calculated from the slope of the $\langle \Delta z^2 \rangle(t)$ curves via (12). The diffusivities of tracers, spheres, and platelets are plotted in Figure 10. For rigid particles, the simulation is carried out between $t = 0$ to 1000. The $\langle \Delta z^2 \rangle$ curves for every time interval of 200 are calculated and then averaged, and the error bars in the figure are the standard deviation of D_z.

The variation of D_z with Ca follows a similar trend as that of τ in the tank-treading regime because of the relatively small variation of $\langle w^2 \rangle$. The diffusivity is thus non-monotonic with the capillary number, and the minimum occurs at $\mathrm{Ca} \approx 0.5$ similar to τ. The size effect is significant for the rigid spherical particles, whose D_z can be higher than that of tracers by more than 50%; better understanding of this phenomenon warrants future investigation. Except for spheres at $\mathrm{Ht} = 0.2$, the diffusivity curves plateau at $\mathrm{Ca} > 1$, which is consistent with the saturation of the cell deformation. The dimensional $D_z^* = \dot{\gamma}^* a^{*2} D_z$ thus scales linearly with the shear rate at high Ca. We also note an augmented D_z when Ht increases from 0.1 to 0.2, for which the growth in $\langle w^2 \rangle$ is the dominant effect.

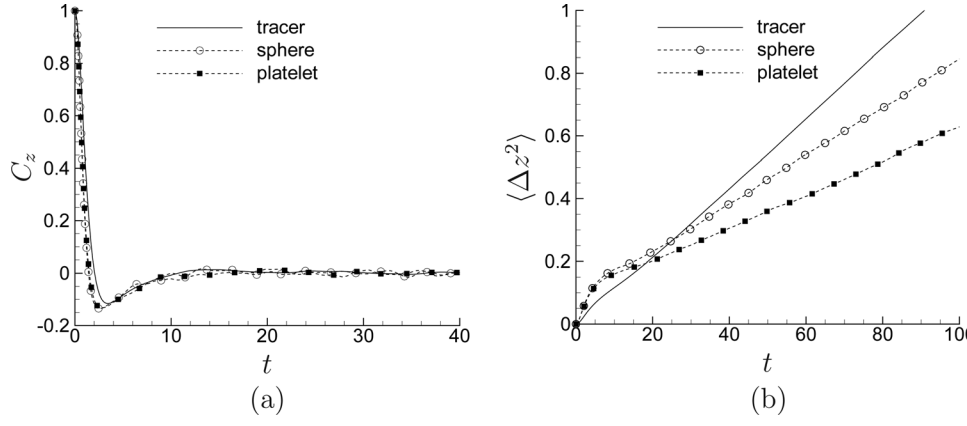

FIG. 9. (a) The z velocity autocorrelation. (b) The mean square displacement of tracers, spheres, and platelets in a bulk shear flow at $\mathrm{Ht} = 0.2$ and $\mathrm{Ca} = 1.2$.

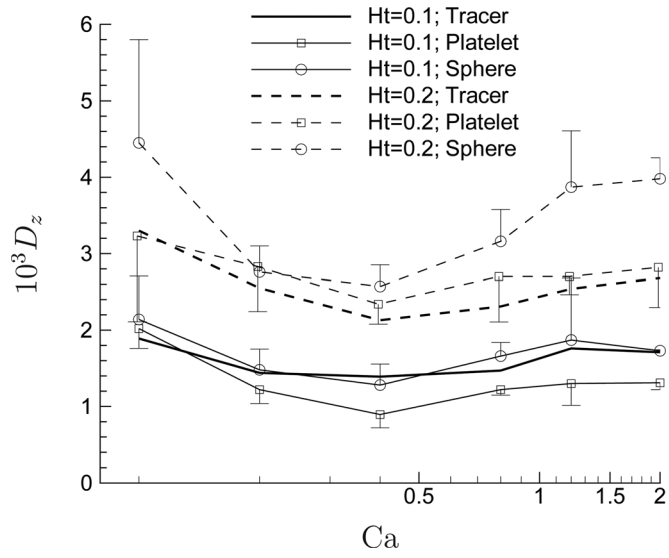

FIG. 10. The self-diffusivity of tracers, spheres, and platelets in the RBC suspension under bulk shear.

Experimentally, the diffusivity of platelets in blood has been determined by measuring their adhesion rate to the subendothelial wall of a perfusion chamber. The diffusivity is obtained by fitting the adhesion rate with the theoretical predictions based on a transport model of the boundary-layer type.[16,17] The diffusivities obtained this way are usually with large uncertainties. Turitto and Baumgartner report $D^* = 2.0 \times 10^{-7}\,\mathrm{cm}^2/\mathrm{s}$ at $\dot{\gamma}_w = 208\,\mathrm{s}^{-1}$, and $D^* = 3.4 \times 10^{-7}\,\mathrm{cm}^2/\mathrm{s}$ at $\dot{\gamma}_w = 832\,\mathrm{s}^{-1}$ for an unknown hematocrit. These translate to the nondimensional $D = 1.2 \times 10^{-2}$ at $\mathrm{Ca} = 0.1$, and $D = 5.1 \times 10^{-3}$ at $\mathrm{Ca} = 0.4$. Aarts *et al.* however obtain much lower platelet diffusivities from similar perfusion chamber experiments and the same data fitting procedure.[17] Using their empirical power law of $D^* \propto \dot{\gamma}_w^{*0.54\pm0.03}$ at $0.1 \le \mathrm{Ca} \le 0.6$ and $\mathrm{Ht} = 0.2$, the nondimensional diffusivity is $D = 1.2 \times 10^{-3}$ at $\mathrm{Ca} = 0.1$ and is 6.2×10^{-4} at $\mathrm{Ca} = 0.4$. The platelet diffusivity $D_z \approx 2.5 \times 10^{-3}$ at $\mathrm{Ca} = 0.4$ in our simulation lies between the two experimental estimates.

IV. PARTICLE MIGRATION IN A MICROCHANNEL

The simulation of RBCs and platelets flowing in a microchannel is visualized in Figure 2. The 34 μm channel height is characteristic of those found in venules and arterioles. Nondimensionalized by the RBC radius, the channel has a streamwise length $L = 16$ and a height $H = 12$; the spanwise depth is $W = 9$ that is more than 3 times the RBC diameter and is adequate for fully three-dimensional flow development as discussed in Sec III. Periodic velocity boundary conditions are applied in the x and y directions, while the fluid velocity at the wall boundary is constrained to be zero by explicitly solving the wall friction force in Eq. (5). The characteristic shear rate is defined as $\dot{\gamma}^* = 6\langle u \rangle^*/H^*$, which corresponds to the wall shear rate of a parabolic Poiseuille flow with the same mean velocity $\langle u \rangle^*$. The mean channel hematocrit $\langle \mathrm{Ht} \rangle$ is chosen to be 0.1 and 0.2: $\mathrm{Ht} = 0.2$ is a physiologically relevant value due to the reduction of the local hematocrit in small vessels, while the even lower $\mathrm{Ht} = 0.1$ is to emulate the conditions of blood loss or anemia, for which it has been observed that the decrease in local hematocrit is correlated with longer bleeding time.[5,41]

Since the channel height is only about four times that of the RBC diameter, the flow is obviously highly inhomogeneous in the wall normal direction. At $\mathrm{Ca} = O(1)$ and with an initial random disposition of undeformed cells, more than 50 flow through times (i.e., $L/\langle u \rangle$) are typically necessary to establish a stationary hematocrit profile in space. This corresponds to a relaxation time scale of about 400, which is of the same order as the relaxation time scale $(H/a)^3 a/\langle u \rangle = 864$ for the channel flow of rigid spheres.[42]

The instantaneous configurations (after the distribution is stationary) of the cellular suspension at $\mathrm{Ca} = 0.25$, 0.5, and 2 are shown in Figure 11. The cell-free layer is clearly visible in all the

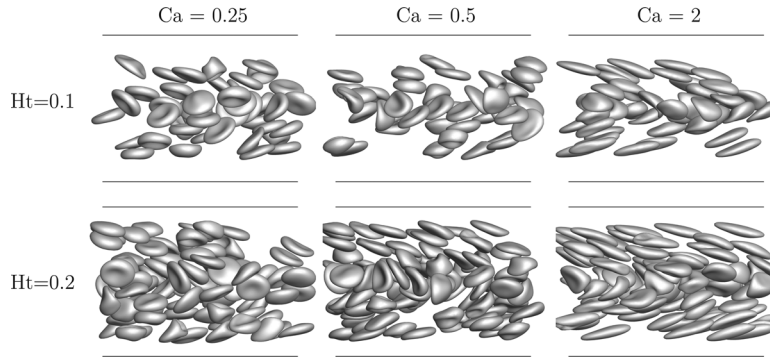

FIG. 11. RBC suspensions flowing in a microchannel.

cases, and its thickness is reduced when hematocrit increases from 0.1 to 0.2. In the near-wall region where the local shear rate is the highest, the cells start to tank-tread with a more uniform inclination angle distribution at $\mathrm{Ca} \geq 0.5$, similar to what is found in a bulk shear flow. The effect of velocity curvature becomes significant at the centerline, where the cells form slipper-like shapes similar to those in a capillary tube.[43]

To calculate the hematocrit profile in the channel, we divide the channel into 24 intervals of equal size in the z direction and use the cell volume enclosed within each interval to calculate the mean local hematocrit. The time-averaged profiles are shown in Figure 12, where the maximal Ht occurs at the centerline, and its peak value increases slightly with Ca but stops increasing at $\mathrm{Ca} > 1$.

The hematocrit profiles in Figure 12 also indicate the insensitivity of the cell-free layer thickness to Ca, which is consistent with observations from *in vivo* experiments.[44–46] Alternatively, we can define locally a cell-free layer thickness for any point on the channel wall—that is, the maximal vertical distance into the flow before the surface of a red blood cell is reached.[47] Figure 13 shows the normalized probability density distribution of the cell-free layer thickness defined this way. At the highest $\mathrm{Ca} = 2$, the cell-laden region is slightly more compressed toward the centerline, but the variation between curves at different Ca is small. At $\mathrm{Ht} = 0.1$, the high probability at $z = H/2$ means that for a large portion of the channel wall, there are no RBCs between them and the centerline. This apparent porosity of the RBC suspension is consistent with the observation of Fedosov *et al*.[47] Simulation of RBCs flowing in a cylindrical tube of 12 μm diameter has also confirmed that the thickness of the layer is independent of flow rate when the wall shear rate is above $100\,\mathrm{s}^{-1}$.[37] Kameneva *et al*. report a power-law growth of the thickness with flow rate where the

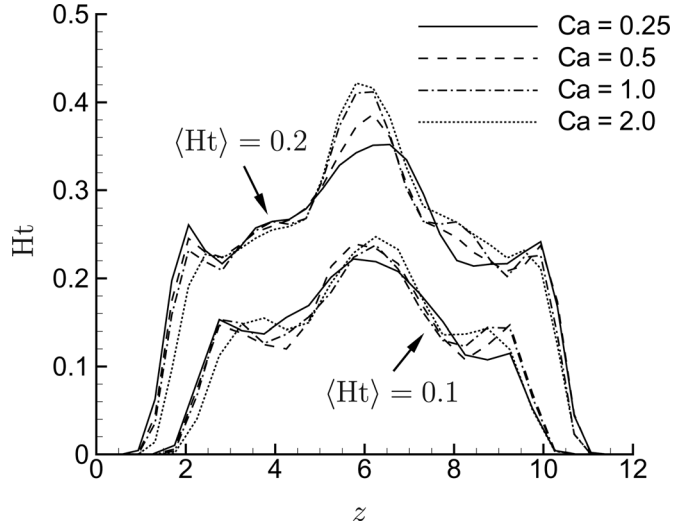

FIG. 12. The hematocrit profiles of the channel flow in the wall normal direction.

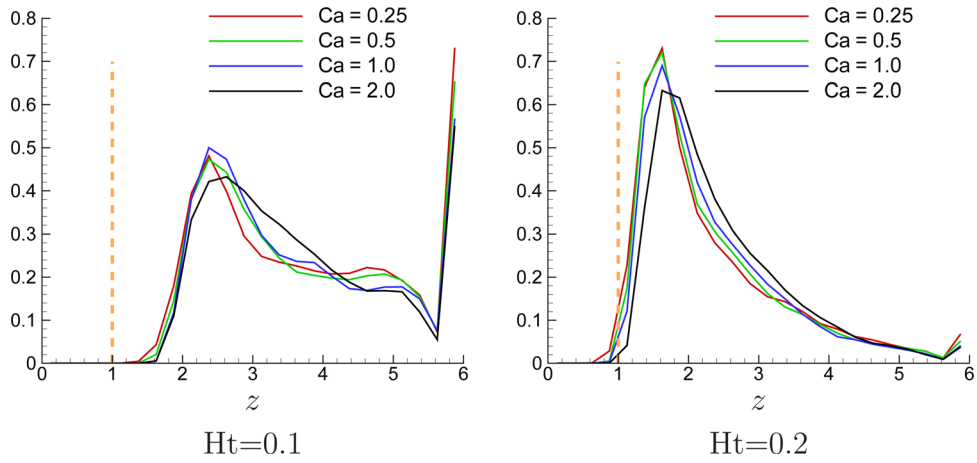

FIG. 13. (Color online) The histogram of the cell-free layer thickness. The dashed vertical line denotes the diameter of the platelet.

measurement is done in a microchannel of $100 \times 100\,\mu$m cross section; however the shear rates are much higher than those in our simulation (between $10^3\,\mathrm{s}^{-1}$ and $5 \times 10^4\,\mathrm{s}^{-1}$ by our estimation), and the Reynolds number is non-negligible (up to 20).[48]

If we consider the first layer of cells beyond the wall, they experience an upward lift velocity due to the hydrodynamic interaction with the wall and a downward repulsion due to collisions with cells that are closer to the centerline. The equilibrium position in z is obviously determined by the balance between these two competing effects. If the cell is well separated from the wall, the lift velocity follows the scaling law of $u_{\mathrm{lift}} \propto S_{zz}/h^2$, where S_{zz} is the wall-normal component of the particle stresslet and h is the centroid height away from the wall.[8] Because the membrane is incompressible, the particle stresslet is almost linearly proportional to the shear rate,[49] especially at high Ca. The specific scaling of $u_{\mathrm{lift}} \propto S_{zz}/h^2$ does not apply at close contact, i.e., when h is comparable to a and lubrication dominates. Nevertheless, numerical simulations suggest that u_{lift} still scales linearly with shear rate in this regime due to the membrane's incompressibility.[50] On the other hand, the effective repulsive velocity, which is from cell–cell collisions, is proportional to the collision frequency and thus scales linearly with shear rate. Because the two competing effects have the same linear scaling with the shear rate, the equilibrium height of the first layer of RBCs, and in turn the cell-free layer thickness, must be insensitive to shear rate or Ca.

With respect to the reference shear rate $\dot{\gamma}^* = 6\langle u^* \rangle / H^*$, the wall shear rate $\dot{\gamma}_w$ for $\mathrm{Ht} = 0.2$ decreases from 1.22 at $\mathrm{Ca} = 0.25$ to 1.13 at $\mathrm{Ca} = 2$. The shear thinning is weaker at $\mathrm{Ht} = 0.1$, where $\dot{\gamma}_w$ changes from 1.07 to 1.04 for the same change in Ca. The mean axial velocities, when normalized by $\dot{\gamma}_w a$ as shown in Figure 14, collapse to the same Poiseuille flow profile in the cell-

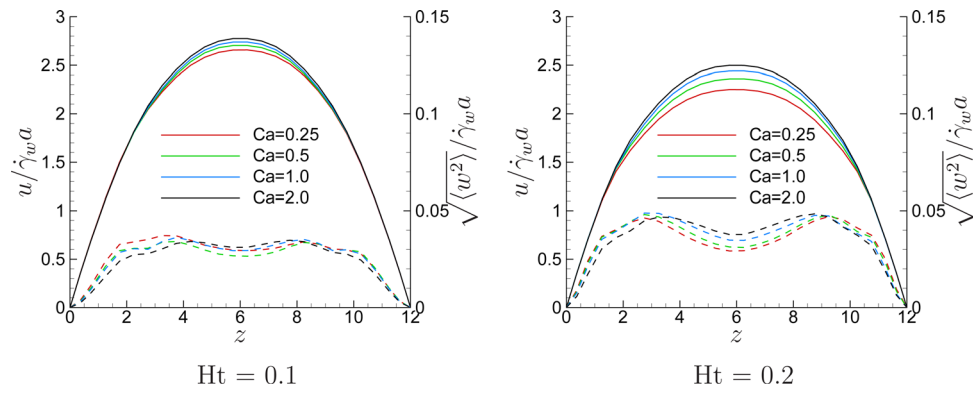

FIG. 14. (Color online) The mean axial velocity (solid line) and the root mean square of wall normal velocity fluctuation (dashed lines), with both normalized by the wall shear velocity $\dot{\gamma}_w a$. The profiles of platelets follow closely those of the tracer points shown here (Ref. 51).

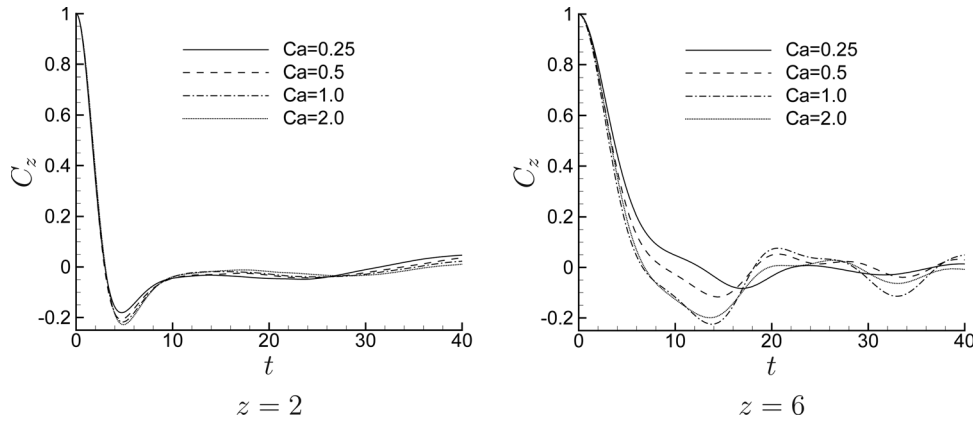

FIG. 15. The velocity autocorrelation of tracers at $z = 2$ and $z = 6$ for channel flow at system Ht = 0.1.

free layer. The velocity profiles become blunt in the cell-laden region, and the deviation from the parabolic profile is more significant with decreasing Ca and increasing Ht, as both cause the effective viscosity to increase. We have shown previously that the profiles of the x velocity and $\sqrt{\langle w^2 \rangle}$ of platelets closely follow those of the tracer points.[51]

Figure 14 shows that $\sqrt{\langle w^2 \rangle}$ vanishes at the wall because of the no-slip boundary condition and increases monotonically away from the wall in the cell-free layer. The maximum of $\sqrt{\langle w^2 \rangle}$ occurs right beyond the first layer of cells away from the wall; it then reduces as the centerline is approached but remains nonzero at the centerline despite the zero local mean shear rate. A nearly zero $\sqrt{\langle w^2 \rangle}$ at the centerline would have resulted if the cells were of parachute shapes with their axes of symmetry coincident with the centerline.[52] Under such configurations, the cells undergo pure rigid-body translation without membrane tank treading. However, it is clear from Figure 11 that the cells instead have asymmetric slipper-like shapes,[43] especially at high Ca numbers. Therefore, the membrane's tank treading motion persists and induces nonzero disturbance velocity in the surrounding fluid. The observation is similar to the non-vanishing suspension temperature (which is proportional to the mean square of the disturbance velocity) at the centerline for channel flow laden with rigid spheres.[42] The $\sqrt{\langle w^2 \rangle}$ increases with the system hematocrit, similar to that in a bulk shear flow.

The channel is uniformly divided into 12 intervals in the z direction for calculating the velocity autocorrelation of Lagrangian tracer points. For time interval $[t, t + \Delta t]$, the autocorrelation $w(t)w(t + \Delta t)$ of any tracer point is assigned to the z interval within which the tracer lies at time t. Figure 15 shows the normalized autocorrelation curves for Ht = 0.1 at $z = 2$ in the cell-free layer and $z = 6$ at the channel center. Because of its higher local shear rate, the characteristic decay time of $C_z(t)$ at $z = 2$ is much smaller than at $z = 6$. At $z = 6$, the initial decorrelation occurs at similar rates for all Ca, but the negative minima of the correlation deepens as Ca increases, which will have a negative impact on the integral time scale and thus the effective diffusivity. Because of the very weak shear thinning effect at Ht = 0.1, there is no need to rescale the time for different Ca. At Ht = 0.2, the curves overlap well only when t is scaled by a local shear rate.[51]

In Figure 16, we compare the velocity autocorrelations in a channel flow with that in a bulk shear flow, both at Ht = 0.2. The channel flow has Ca = 2, and the autocorrelation curve is for the $z = 3$ plane that is within the cell-laden region but is still reasonably far away from the centerline. The capillary number based on the local mean shear rate is 0.79, so is close to the Ca = 0.8 in the bulk shear flow. The two curves share similar features despite the clear quantitative difference—there is still a significant velocity curvature effect here because the local shear rate has $O(1)$ change over the vertical distance of one RBC diameter.

From the characteristics of their velocity autocorrelation (cf. Figure 15), it is clear that the integral time scale τ of tracer points must decrease with increasing Ca in the core flow region, which is the opposite of the Ca-dependence of τ in the bulk shear flow. Nevertheless, at Ca ≥ 1, τ becomes largely independent of Ca in both flow environments. Figure 17 demonstrates the

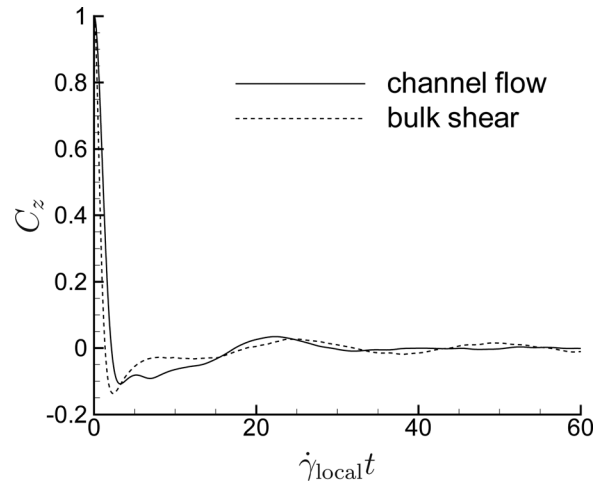

FIG. 16. The velocity autocorrelations of tracers in a bulk shear flow of Ca = 0.8 and in a channel flow of Ca = 2. For the latter, the capillary number based on the local mean shear rate is 0.79.

reduction of the integral time scale with increasing Ca in the cell-laden region, where the most significant decay of τ occurs at Ca < 1. The integral time scale is reduced at higher hematocrit, following the same trend as that in the bulk shear flow.

Because the variation of $\langle w^2 \rangle$ with Ca is small, the particle diffusivity in the cell-laden region follows the same trend as the integral time scale τ. Figure 18 shows that D_z decreases with increasing Ca but levels off when Ca > 1. When the linear growth of $\langle \Delta z^2 \rangle$ with t is established in the cell-laden region, the spread width of the particles has become comparable to the width of this region. Because of this, we have calculated D_z by averaging the $\langle \Delta z^2 \rangle$ curves over the entire cell-laden region, which also results in better statistics.

Saadatmand *et al*. measure the dispersion of microbeads of 1 μm diameter in an RBC suspension flowing through a cylindrical tube of 50 μm diameter.[18] The size of the cross section is similar to that in our simulation, but the Ca in the experiment is less than 0.1. In agreement with the present numerical results, the radial migration of the beads near the channel wall is found to be much slower than that in the core flow region. The diffusivity of the beads, as determined from their mean square displacement in the radial direction, is reported to be proportional to the shear rate, and thus the nondimensional $D_z = 3.6 \times 10^{-3}$ is independent of Ca. This value is close to $D_z = 2.5 \times 10^{-3}$ for the tracer points at the lowest Ca = 0.25 in our simulation, although our simulations suggest a sublinear scaling of D_z^* with shear rate at this small Ca.

In their two-dimensional lattice Boltzmann simulation of platelets/RBCs in a channel of 50 μm height, Crowl and Fogelson find that the D_z of platelet is almost uniform in the core flow

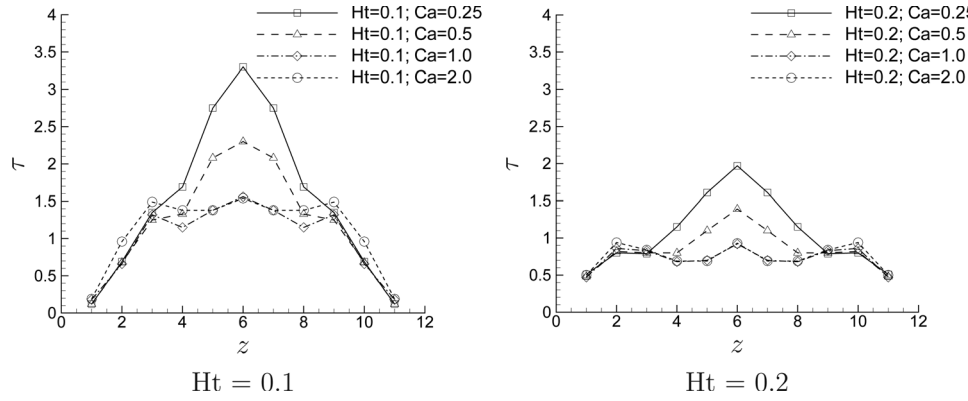

FIG. 17. The profile of the integral time scale τ of tracer points in the channel flow.

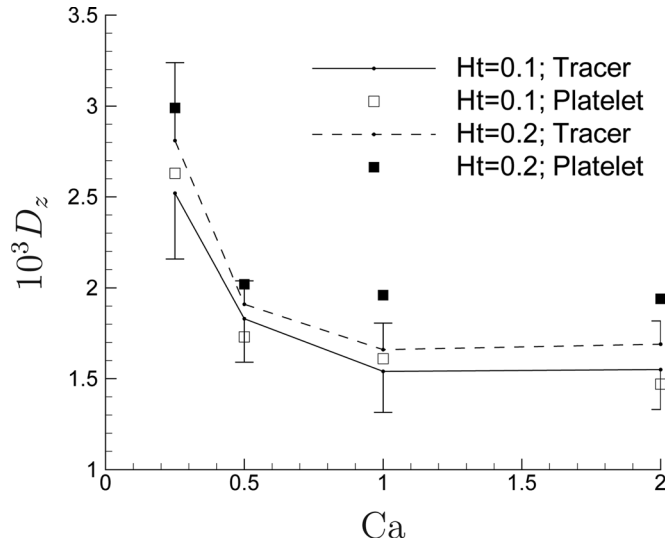

FIG. 18. The self-diffusivity of tracer points and platelets in the cell-laden region of the channel.

region.[13] At Ht = 0.2 and $\dot{\gamma}_w^* = 1100\,\mathrm{s}^{-1}$, they obtain $D_z^* \approx 2 \times 10^{-6}\,\mathrm{cm}^2\,\mathrm{s}^{-1}$. This translates to a dimensionless $D_z \approx 2.3 \times 10^{-2}$, which is an order of magnitude higher than the values from our three-dimensional simulations. In three dimensions, the RBC and platelet in a collision can have different centroid coordinates in the vorticity direction. The collision will then result in a smaller platelet displacement than that from a perfectly in-plane collision, which is always the case in two dimensions. We suspect that the difference in the particle diffusivity can be attributed to this effect.

The shear-induced diffusivity causes the spreading of particles in the cell-laden region. However, pure diffusion alone, even with a spatially varying diffusivity, can only result in a uniform particle distribution instead of the observed density peaks in the cell-free layer. Crowl and Fogelson find a net drift velocity of platelets that drives platelets toward the wall.[13] A similar mean lateral velocity is also evident in the current three-dimensional simulations, and Figure 19 shows profiles of the platelet mean wall normal velocity $\langle w \rangle$. Compared with its fluctuation $\sqrt{\langle w^2 \rangle}$, the $\langle w \rangle$ is smaller by one order of magnitude. The maximum $\langle w \rangle$ occurs near the edge of the cell-free layer: a platelet in this region experiences more collisions with RBCs from the centerline side than with those from the wall side, and the mean lateral velocity emerges as a result of the asymmetry of the collisions.[13] The profiles of $\langle w \rangle$ here is qualitatively similar to those observed in two dimensions, but like the diffusivity, the magnitude is smaller by about 10 times.

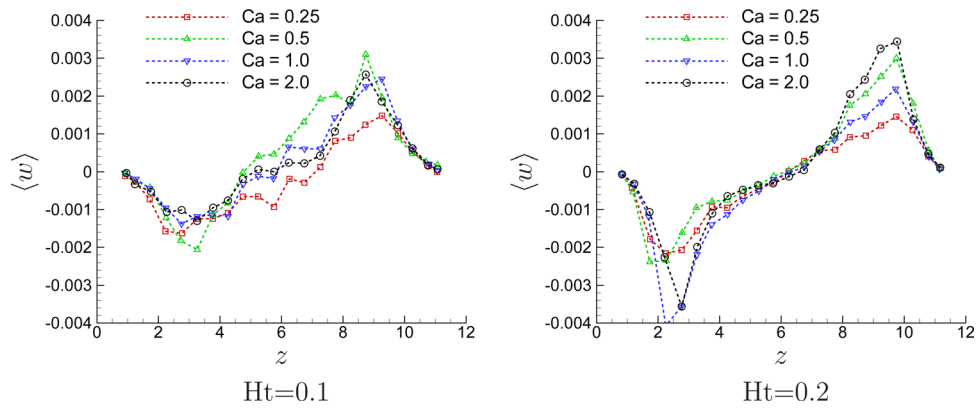

FIG. 19. (Color online) The mean wall normal velocity of platelets in the channel flow.

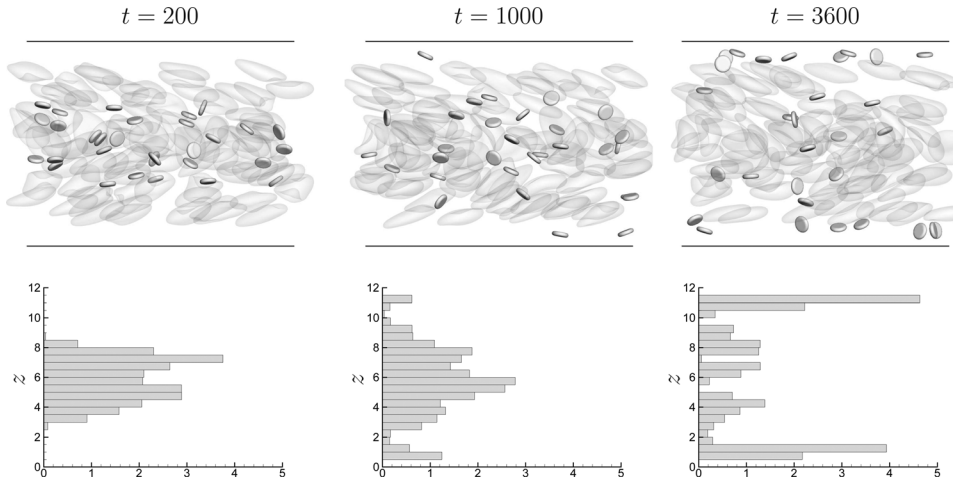

FIG. 20. The evolution of the platelet distribution in the channel. Ht = 0.2 and Ca = 0.5.

Passive Lagrangian tracer points do not exhibit any mean lateral drift at a stationary state, even though their self-diffusivity is close to that of the platelets. Because these tracer points follow the extracellular plasma velocity, any drift in the wall normal direction—if it does exist—must be balanced by a net drift of RBCs in the opposite direction as dictated by mass conservation, which is not possible after the flow has reached a stationary state. The qualitative difference in $\langle w \rangle$ between tracer points and platelets means that $\langle w \rangle$ must strongly depend on the size and the shape of the particle. Opposite to the Ca-dependence of the diffusivity, $\langle w \rangle$ appears to increase with Ca in Figure 19, but the trend is not strictly monotonic (note the peak of $\langle w \rangle$ at Ca = 0.5 exceeds that at Ca = 1.0 near $z = 10$). More investigation is necessary to make a clear conclusion.

The lateral migration of platelets in the channel flow can thus be phenomenologically modeled as a convection and diffusion process. When platelets are initially released near the centerline, they spread out laterally due to the dominant shear-induced diffusion in the cell-laden region; and they are further driven toward the wall by the mean lateral velocity. Figure 20 shows snapshots of platelet number density distributions. The platelet margination is clearly visible and appears irreversible, as the very small velocity fluctuations near the wall and the mean lateral velocity make it difficult for the platelets to re-enter the cell-laden region. The comparison between the density profiles at $t = 200$ and $t = 3600$ shows that more than half of the platelets have migrated to the cell-free layer at $t = 3600$ (Figure 20). The asymmetry in the platelet density profile is caused by the bias in the initial platelet distribution that is difficult to control precisely. Comparing the density profiles at Ht = 0.1 in Figure 21 with those at Ht = 0.2 in Figure 20, we

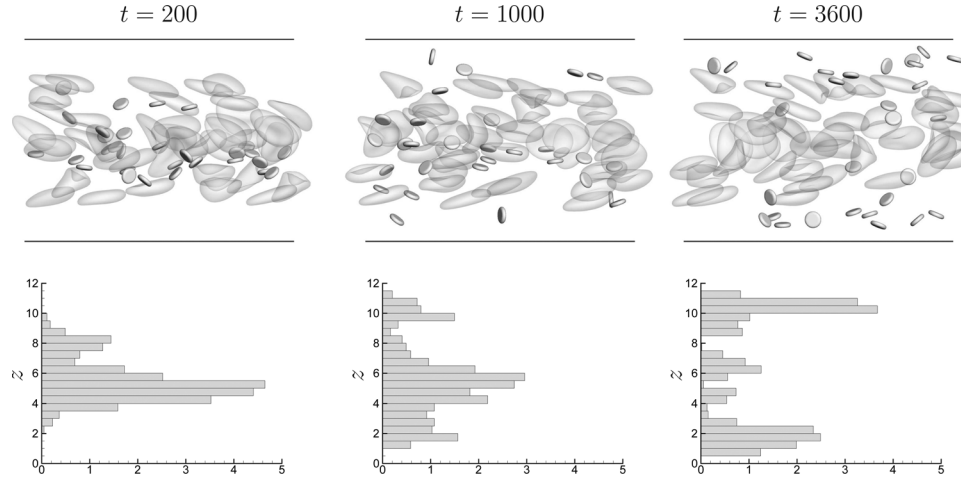

FIG. 21. The evolution of the platelet distribution in the channel. Ht = 0.1 and Ca = 0.5.

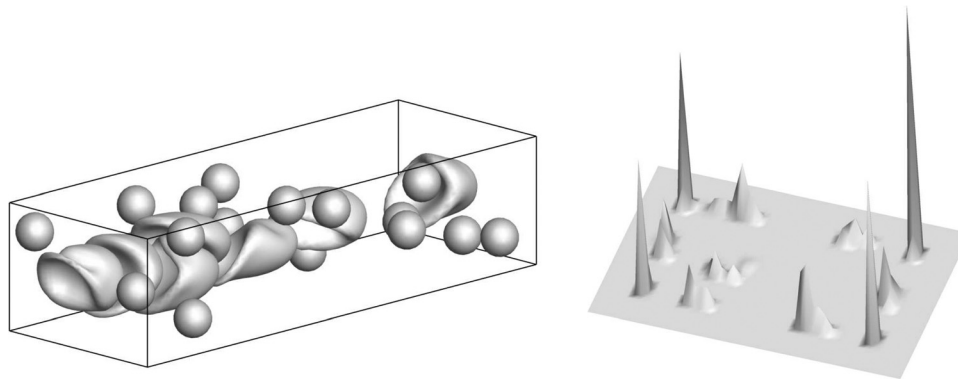

FIG. 22. Left: RBCs and beads of 3 μm-diameter in a rectangular channel of 10×15 μm cross section. Right: the beads number density profile in the channel cross section from our simulation.

find that at lower mean hematocrit, the profiles in the cell-free layer are wider and have lower peak values obviously because of thickening of the cell-free layer. In the case of vessel injury, a platelet in the cell-free layer will then have to travel longer on average in the wall normal direction to reach the vessel wall at a lower hematocrit. The smaller $\langle w^2 \rangle$ in the cell-free layer at $\mathrm{Ht} = 0.1$ also means slower migration if the platelet reaches the endothelium through diffusion. These are likely causes of the positive correlation between lowered hematocrit and longer bleeding time.[5]

For a platelet that is initially at a random position of the cell-laden region, we estimate its convection distance to be $\langle u \rangle (H/4)^2/D_z$ before it migrates into the Fahraeus–Lindquist layer via diffusion. At $\mathrm{Ht} = 0.2$ and $\mathrm{Ca} = 1$, this gives a convection distance of about 30 mm, which is 60 times larger than the average vessel branch (about 500 μm) at this diameter.[53] Therefore, the flow at the branching of blood vessels may play an important if not dominant role in determining the platelet concentration profile in the microvascular network.

V. SEPARATION OF RED CELLS AND RIGID SPHERICAL BEADS IN A 10×15 μM DUCT

In vessels of sizes comparable to the RBC diameter, the RBCs deform into slipper-like or umbrella-like shapes under high shear rate and migrate toward the centerline. On the other hand, rigid spheres in a Poiseuille flow alone do not migrate laterally due to its fore-aft symmetry. Figure 22 shows our simulation of RBCs and spherical beads (3 μm in diameter) flowing in a rectangular channel of 10×15 μm cross section—the same configuration as the experiments reported by Hou *et al.*[54] The wall shear rate is about $1000\,\mathrm{s}^{-1}$, and the mean hematocrit is 0.1. The deformed RBCs form a single-profile train at the duct center where the axial velocity is maximal, and they push the nearby beads toward the corners of the duct. The bead margination is thus predominantly due to volume exclusion and occurs almost instantaneously within a time scale of $O(10)$, as compared to $O(10^3)$ for the platelets in the larger channel that is discussed in Sec IV.

The segregation between deformable cells and stiffened cells in a channel flow is reported previously, in which the stiffer cells migrate from their initial positions near the centerline to the peripheral of the cell-laden region.[23] The side length of the channel cross section in that study is more than 4 times the cell diameter and much bigger than the one discussed here, and thus the migration of the cells in that study is dominated by the slower diffusion which occurs at a time scale of $O(10^3)$.

The channel/duct flow systems discussed here are analogous to the endothelial wall-adhesion of sickled or malaria-infected RBCs.[55,56] Despite their distinct pathology, these cells have more irregular shapes and stiffened membranes than normal RBCs,[57] which lead to their severely reduced deformability. The simulation suggests that these rigid cells will be expelled toward the vessel walls due to volume exclusion or by shear-induced diffusion/convection depending on the vessel size. Furthermore, because of the much enhanced speed of margination in smaller vessels, a rigidified RBC will migrate to the endothelium with a streamwise traveling distance of only 10

cell diameters after exiting a capillary. This statement is consistent with observations that the endothelial wall adhesion occurs predominantly in postcapillary vessels.[58,59]

VI. CONCLUSION

We have simulated the cross-flow migration of rigid particles in a red blood cell suspension in two distinct flow environments: (1) a suspension undergoing bulk shear motion and (2) a suspension flowing in a microchannel. The particle migration in these systems is characterized by their shear-induced diffusion and/or a mean lateral velocity both due to the hydrodynamic interactions between particles and RBCs.

In a bulk shear flow, the characteristics of the particle's velocity fluctuation are closely related to the alignment of RBCs in the suspension, and the autocorrelation decays more slowly at high capillary number. We observe a non-monotonic behavior of the dimensionless diffusivity with the increase of Ca because of the competition between the decaying $\langle w^2 \rangle$ and the growing integral time scale τ.

In a microchannel flow, the velocity fluctuations created by RBCs cause the platelets to spread diffusively in the cell-laden region. The nondimensional shear-induced diffusivity of platelets decreases monotonically with increasing flow Ca because the integral time scale decreases significantly with increasing Ca. A mean lateral velocity further expels the platelets toward the wall, causing their accumulation in the cell-free layer.

For both flow environments, the effect of Ca on the suspension velocity fluctuations is most significant near $\mathrm{Ca} \approx 0.5$, which is roughly the onset of a tank-treading motion of RBCs. At higher Ca, the cell deformation saturates and so do other flow-related quantities such as the particle diffusivity. The interactions between RBCs dominate the velocity fluctuations, hence the platelets and Lagrangian tracer points have similar diffusivities. On the other hand, the particle mean lateral velocity in the channel flow must depend on the particle size and shape, which warrants further investigation.

For RBCs and rigid spheres flowing in a duct of capillary size, the RBCs form a single-profile train close to the duct centerline, and they push the spheres outward to the corners of the duct. The segregation is dominated by volume exclusion, and occurs $O(100)$ times faster than the diffusional migration in the larger channel. The implication to the RBC–endothelium adhesion as observed in malaria or sickle cell disease is discussed.

ACKNOWLEDGMENTS

The authors thank the support from the U.S. Army High Performance Computing Research Center (AHPCRC) and the support from Stanford University's Certainty computer cluster that is funded by the American Recovery and Reinvestment Act (ARRA) of 2009. V.N. is supported by the NSF through a Graduate Research Fellowship.

[1]P. A. Aarts, S. A. van den Broek, G. W. Prins, G. D. Kuiken, J. J. Sixma, and R. M. Heethaar, "Blood platelets are concentrated near the wall and red blood cells, in the center in flowing blood," Arterioscler. Thromb. Vasc. Biol. **8**, 819 (1988).
[2]A. W. Tilles and E. C. Eckstein, "The near-wall excess of platelet-sized particles in blood flow: Its dependence on hematocrit and wall shear rate," Microvasc. Res. **33**, 211 (1987).
[3]V. T. Turitto and H. J. Weiss, "Red blood cells: their dual role in thrombus formation," Science **207**(4430), 541 (1980).
[4]M. Small, G. D. O. Lowe, E. Cameron, and C. D. Forbes, "Contribution of the haematocrit to the bleeding time," Haemostasis **13**, 379 (1983).
[5]C. R. Valeri, G. Cassidy, and L. E. Pivacek, "Anemia-induced increase in the bleeding time: implications for treatment of nonsurgical blood loss," Transfusion **41**, 977 (2001).
[6]J. A. Champion, Y. K. Katare, and S. Mitragotri, "Particle shape: A new design parameter for micro- and nanoscale drug delivery carriers," J. Controlled Release **121**, 3 (2007).
[7]S. Muro, C. Garnacho, J. A. Champion, J. Leferovich, C. Gajewski, E. H. Schuchman, S. Mitragotri, and V. R. Muzykantov, "Control of endothelial targeting and intracellular delivery of therapeutic enzymes by modulating the size and shape of ICAM-1-targeted carriers," Mol. Ther. **16**(8), 1450 (2008).
[8]J. R. Smart and D. T. Leighton, "Measurement of the drift of a droplet due to the presence of a plane," Phys. Fluids A **3**(1), 21 (1991).
[9]R. Fahraeus and T. Lindqvist, "The viscosity of blood in narrow capillary tubes," Am. J. Physiol. **96**, 562 (1931).
[10]C. Pozrikidis, "Orbiting motion of a freely suspended spheroid near a plane wall," J. Fluid Mech. **541**, 105 (2005).

[11]E. C. Eckstein, D. G. Bailey, and A. H. Shapiro, "Self-diffusion of particles in shear flow of a suspension," J. Fluid Mech. **79**(1), 191 (1977).
[12]D. Leighton and A. Acrivos, "The shear-induced migration of particles in concentrated suspensions," J. Fluid Mech. **181**, 415 (1987).
[13]L. Crowl and A. L. Fogelson, "Analysis of mechanisms for platelet near-wall excess under arterial blood flow conditions," J. Fluid Mech. **676**, 348 (2011).
[14]C. Yeh and E. C. Eckstein, "Transient lateral transport of platelet-sized particles in flowing blood suspensions," Biophys. J. **66**, 1706 (1994).
[15]R. Zhao, M. V. Kameneva, and J. F. Antaki, "Investigation of platelet margination phenomena at elevated shear stress," Biorheology **44**, 161177 (2007).
[16]V. T. Turitto and H. R. Baumgartner, "Platelet deposition on subendothelium exposed to flowing blood: mathematical analysis of physical parameters," Trans. Am. Soc. Artif. Intern. Organs **21**, 593 (1975).
[17]P. A. Aarts, P. Steenduk, J. J. Sixma, and R. M. Heethaar, "Fluid shear as a possible mechanism for platelet diffusivity in flowing blood," J. Biomech. **19**(10), 799 (1986).
[18]M. Saadatmand, T. Ishikawa, N. Matsuki, M. J. Abdekhodaie, Y. Imai, H. Ueno, and T. Yamaguchi, "Fluid particle diffusion through high-hematocrit blood flow within a capillary tube," J. Biomech. **44**, 170 (2011).
[19]T. AlMomani, H. S. Udaykumar, J. S. Marshall, and K. b. Chandran, "Micro-scale dynamic simulation of erythrocyte–-platelet intereaction in blood flow," Ann. Biomed. Eng. **36**(6), 905 (2008).
[20]E. W. Merrill, "Rheology of blood," Physiol. Rev. **49**(4), 863 (1969).
[21]C. Sun and L. L. Munn, "Influence of erythrocyte aggregation on leukocyte margination in postcapillary expansions: A lattice Boltzmann analysis," Physica A **362**, 191 (2006).
[22]J. B. Freund, "Leukocyte margination in a model microvessel," Phys. Fluids **19**, 023301 (2007).
[23]L. L. Munn and M. M. Dupin, "Blood cell interactions and segregation in flow," Ann. Rev. Biomed. Eng. **36**(4), 534 (2008).
[24]A. Michelson, *Platelets*, 2nd ed. (Academic, Waltham, Massachusetts, 2006).
[25]C. Pozrikidis, *Boundary Integral and Singularity Methods for Linearized Viscous Flow* (Cambridge University Press, Cambridge, 1992).
[26]R. B. Gennis, *Biomembranes: Molecular Structure and Function* (Springer, New York, 1989).
[27]H. Hashimoto, "On the periodic fundamental solutions of the Stokes equations and their application to viscous flow past a cubic array of spheres," J. Fluid Mech. **5**, 317 (1959).
[28]D. Saintillan, E. Darve, and E. S. G. Shaqfeh, "A smooth particle-mesh Ewald algorithm for Stokes suspension simulations: The sedimentation of fibers," Phys. Fluids **17**, 033301 (2005).
[29]H. Zhao, A. H. G. Isfahani, L. Olson, and J. B. Freund, "A spectral boundary integral method for micro-circulatory cellular flows," J. Comput. Phys. **229**(10), 3726 (2010).
[30]R. Skalak and N. Ozkaya, "Biofluid mechanics," Annu. Rev. Fluid Mech. **21**, 167 (1989).
[31]C. Pozrikidis, "Numerical simulation of the flow-induced deformation of red blood cells," Ann. Biomed. Eng. **31**, 1194 (2003).
[32]J. Li, M. Dao, C. T. Lim, and S. Suresh, "Spectrin-level modeling of the cytoskeleton and optical tweezers stretching of the erythrocyte," Biophys. J. **88**, 3707 (2005).
[33]I. V. Pivkin and P. E. Karniadakis, "Accurate coarse-grained modeling of red blood cells," Phys. Rev. Lett. **101**, 118105 (2008).
[34]J. P. Mills, L. Qie, M. Dao, C. T. Lim, and S. Suresh, "Nonlinear elastic and viscoelastic deformation of the human red blood cell with optical tweezers," Mech. Chem. Biosyst. **1**(3), 169 (2004).
[35]H. H. Lipowsky, S. Kovalcheck, and B. W. Zweifach, "The distribution of blood rheological parameters in the microvasculature of cat mesentery," Circ. Res. **43**(5), 738 (1978).
[36]G. R. Cokelet and H. J. Meiselman, "Rheological comparison of hemoglobin solutions and erythrocyte suspensions," Science **162**, 275 (1968).
[37]J. B. Freund and M. M. Orescanin, "Cellular flow in a small blood vessel," J. Fluid Mech. **25**, 466 (2011).
[38]H. H. Lipowsky, S. Usami, and S. Chien, "*In vivo* measurements of apparent viscosity and microvessel hematocrit in the mesentery of the cat," Microvasc. Res. **19**, 297 (1980).
[39]M. Abkarian, M. Faivre, and A. Viallat, "Swinging of red blood cells under shear flow," Phys. Rev. Lett. **98**, 188302 (2007).
[40]S. Ramanujan and C. Pozrikidis, "Deformation of liquid capsules enclosed by elastic membranes in simple shear flow: large deformations and the effect of fluid viscosities," J. Fluid Mech. **361**, 117 (1998).
[41]G. Escolar, M. Garrido, and R. Mazzara, "Experimental basis for the use of red cell transfusion in the management of anemic–thrombocytopenic patients," Transfusion **28**, 406 (1988).
[42]P. R. Nott and J. F. Brady, "Pressure-driven flow of suspensions: simulation and theory," J. Fluid Mech. **275**, 157 (1994).
[43]H. Noguchi and G. Gompper, "Shape transitions of fluid vesicles and red blood cells in capillary flows," Proc. Natl. Acad. Sci. **102**(40), 14159 (2005).
[44]S. Kim, R. L. Kong, A. S. Popel, M. Intaglietta, and P. C. Johnson, "Temporal and spatial variations of cell-free layer width in arterioles," Am. J. Physiol. Heart Circ. Physiol. **293**(3), H1526 (2007).
[45]P. K. Ong, B. Namgung, P. C. Johnson, and S. Kim, "Effect of erythrocyte aggregation and flow rate on cell-free layer formation in arterioles," Am. J. Physiol. Heart Circ. Physiol. **298**(6), H1870 (2010).
[46]N. Tateishi, Y. Suzuki, M. Soutani, and N. Maeda, "Flow dynamics of erythrocytes in microvessels of isolated rabbit mesentery—cell-free layer and flow resistance," J. Biomech. **27**(9), 1119 (1994).
[47]D. A. Fedosov, B. Caswell, A. S. Popel, and G. E. Karniadakis, "Blood flow and cell-free layer in microvessels," Microcirculation **17**, 615 (2010).
[48]M. V. Kameneva, Z. J. J. Wu, A. Uraysh, B. Repko, K. N. Litwak, T. R. Billiar, M. P. Fink, R. L. Simmons, B. P. Griffith, and H. S. Borovetz, "Blood soluble drag-reducing polymers prevent lethality from hemorrhagic shock in acute animal experiments," Biorheology **41**(1), 53 (2004).
[49]H. Zhao and E. S. G. Shaqfeh, "The dynamics of a vesicle in simple shear flow," J. Fluid Mech. **674**, 578 (2011).
[50]H. Zhao, A. P. Spann, and E. S. G. Shaqfeh, "The dynamics of a vesicle in a wall-bounded shear flow," Phys. Fluids **23**(12), 121901 (2011).

[51]H. Zhao and E. S. G. Shaqfeh, "Shear-induced platelet margination in a microchannel," Phys. Rev. E **83**(6), 061924 (2011).
[52]C. Pozrikidis, "Axisymmetric motion of a file of red blood cells through capillaries," Phys. Fluids **17**, 031503 (2005).
[53]D. Lapi, P. L. Marchiafava, and A. Colantuoni, "Geometric characteristics of arterial network of rat pial microcirculation," Vasc. Res. **45**, 69 (2008).
[54]H. W. Hou, A. A. S. Bhagat, A. G. L. Chong, P. Mao, K. S. W. Tan, J. Han, and C. T. Lim, "Deformability based cell margination—a simple microfluidic design for malaria-infected erythrocyte separation," Lab Chip **10**, 2605 (2010).
[55]O. S. Platt, D. J. Brambilla, W. F. Rosse, P. F. Milner, O. Castro, M. H. Steinberg, and P. P. Klug, "Mortality in sickle cell disease: Life expectancy and risk factors for early death," N. Engl. J. Med. **330**(23), 1639 (1994).
[56]G. B. Nash, E. O'Brien, E. C. Gordon Smith, and J. A. Dormandy, "Abnormalities in the mechanical properties of red blood cells caused by *plasmodium falciparum*," Blood **74**(2), 855 (1989).
[57]S. Usami, S. Chien, P. M. Scholtz, and J. F. Bertles, "Effect of deoxygenation in sickle on blood cell disease rheology," Microvasc. Res. **9**, 324 (1975).
[58]D. K. Kaul, M. E. Fabry, and R. L. Nagel, "Microvascular sites and characteristics of sickle cell adhesion to vascular endothelium in shear flow conditions: Pathophysiological implications," Proc. Natl. Acad. Sci. **86**, 3356 (1989).
[59]D. K. Kaul, E. Finnegan, and G. A. Barabino, "Sickle red cell–endothelium interactions," Microcirculation **16**, 97 (2009).